Importance of Precipitation on the Upper Ocean Salinity Response to Typhoon Kalmaegi (2014)

Fu Liu [1,2], Han Zhang [2,3,*], Jie Ming [1,4,*], Jiayu Zheng [5], Di Tian [2] and Dake Chen [2,3]

[1] Key Laboratory of Mesoscale Severe Weather/MOE and School of Atmospheric Sciences, Nanjing University, Nanjing 210023, China; liufu@sio.org.cn

[2] State Key Laboratory of Satellite Ocean Environment Dynamics, Second Institute of Oceanography, Ministry of Natural Resources, Hangzhou 310012, China; tiandi@sio.org.cn (D.T.); dchen@sio.org.cn (D.C.)

[3] Southern Marine Science and Engineering Guangdong Laboratory (Zhuhai), Zhuhai 519082, China

[4] Joint Center for Atmospheric Radar Research of Centre of Modern Analysis/Nanjing University (CMA/NJU), Nanjing 210023, China

[5] State Key Laboratory of Tropical Oceanography, South China Sea Institute of Oceanology, Chinese Academy of Sciences, Guangzhou 510301, China; jyzheng@scsio.ac.cn

* Correspondence: zhanghan@sio.org.cn (H.Z.); jming@nju.edu.cn (J.M.)

Abstract: Using multiple-satellite datasets, in situ observations, and numerical simulations, the influence of typhoon-induced precipitation on the oceanic response to Typhoon Kalmaegi has been discussed. It is found that the convective system and precipitation distribution of Kalmaegi was asymmetric, which leaded to the asymmetric rainfall at observational stations. The sea surface salinity (SSS) of the buoy to the right of storm track increased with a 0.176 practical salinity units (psu) maximal positive anomaly, while the two buoys on the left side underwent several desalination processes, with a maximum decreases of 0.145 psu and 0.278 psu. Numerical simulations with and without precipitation forcing were also performed. Model results showed that typhoon-induced precipitation can weaken sea surface cooling by approximately 0.03–0.40 °C and suppress the SSS increase by approximately 0.074–0.152 psu. The effect of precipitation can be divided into the direct effect and indirect effect. On one hand, freshwater from precipitation directly dilutes the salinity. On the other hand, when salinity decreases, the ocean stratification will be enhanced, the vertical mixing will be restrained, and then the temperature and salinity can be further affected by weakened vertical mixing.

Keywords: typhoon; precipitation; ocean response; satellite; numerical simulations

1. Introduction

Tropical cyclones (TCs) are cyclonic vortex systems with warm-core structures. TCs with wind speeds over 32.7 m/s in the Northwest Pacific are commonly called typhoons. TCs cause intense vertical mixing in the upper ocean, forming "cold wakes" via carrying cold water upward. The sea surface temperature (SST) cooling is usually 1–6 °C [1–3] and, in some cases, can even reach up to 11 °C [4,5]. In the Northern Hemisphere, the surface cooling is generally biased to the right of TCs' moving direction [6–10]. The warm ocean provides heat and water vapor for TC development, and the intensified TC absorbs more vapor and energy, further strengthening the intensity of TC. This process is often called TC-ocean positive feedback [11,12]. However, a TC cannot infinitely strengthen partly because TC-induced SST cooling inhibits the heat flux and water vapor transport from the ocean to the TC and restricts TC development or even weakens the TC [13–15], which is called TC-ocean negative feedback.

Temperature variations caused by a TC is closely related to salinity variations. Previous studies [16–20] have shown that variations in salinity structure affect the mixed layer temperature by changing the static stability of the upper ocean. A study of the effects of salinity found that freshening of the mixed layer can inhibit downward entrainment of heat and weaken SST cooling by changing the seawater density as well as ocean stratification [19]. In tropical oceans and some other areas, the isothermal layer is thicker than the isopycnic layer, with a high-salinity layer between the two layers, i.e., the salinity barrier layer (BL) [21,22]. The BL inhibits surface cooling via preventing the kinetic energy input of TC penetrated the thermocline and reducing the vertical mixing of cold water, which favors TC development [23–25]. In the Bay of Bengal, it was found that salinity stratification had a remarkable effect on TC intensity: the haline stratification caused a cooling decrease between post-monsoon and pre-monsoon seasons of up to 40%, while thermal stratification accounts for the remaining 60% of the cooling reduction [26]. Therefore, the upper ocean salinity response and its feedback to TCs require further study.

Under the influence of Typhoon Choi-Wan (2009), a mooring to the left side of the TC track showed an increase in salinity in the mixed layer (MLS) [27]. Before and after the passage of Hurricane Gonzalo (2014), an underwater glider observed a salinity increase of 0.6 practical salinity units (psu) in the water above 20 m and a salinity reduction of 0.4 psu between depths of 30 m and 130 m [28]. The sea surface salinity (SSS) response to Hurricane Isaac (2012) studied using microwave remote sensing data presented a freshening signature near the center of the TC [18]. Both mooring observations and remote sensing data showed that the cyclone Phailin (2013) caused a SSS increase on the right side of the track [29]. Argo profiles during Typhoon Tingting (2004) also observed significant MLS freshening; statistics of Argo profiles from 2000 to 2005 found an almost symmetrical variations on two sides of the track [30]. Several observations from moored buoys showed an SSS increase (decrease) to the right (left) of the track [31,32]. Although there have been many studies on the salinity response during TCs, the response symmetry, changing tendency, and other characteristics of the TC-induced salinity response are still uncertain.

The main factors that affect the ocean responses caused by TCs generally include storm intensity [33–35], translation speed [1,33–35] and pre-storm oceanic conditions, such as the mixed layer thickness, which can modulate vertical mixing [36,37], and thermohaline stratification, which modulates vertical advection [28,38,39]. Using numerical model simulations, a complex relationship was found between the BL and TC-induced upper ocean responses. For a weak TC, when its kinetic energy is not enough to spread below the mixed layer, the air-sea heat flux controlled the SST cooling, while the TC is strong enough to trigger strong entrainment into the BL, the heat loss at the sea surface can be partly compensated for by the warmer water in the BL [25].

To some extent, the salinity response is similar with the temperature response. The SSS is mainly affected by five processes: rainfall, evaporation, vertical mixing, entrainment and advection [24,30,40]. Given the pre-storm salinity structure, the final salinity change depends on the competition among those five processes. Generally, seawater salinity increases monotonously with depth. The vertical mixing and entrainment can induce salinity increases in the mixed layer and decreases in deeper layer [1,28,38,39]. A moored buoy captured a slight increase in SSS during cyclone Nargis (2008) caused by intense entrainment of high-salinity subsurface water [41]. The effect of advection varies with the horizontal and vertical gradients of salinity. Generally, downwelling (upwelling) reduces (increases) the salinity at a certain depth. In the study of the upper ocean variation induced by Hurricane Katia (2011), a region where SSS is reduced by approximately 1 psu was found, which was considered to be caused by the horizontal advection of freshwater from a low-SSS plume [42] with the additional contribution of direct rainfall [38]. An analysis based on Argo salinity profiles of typhoons in the Northwest Pacific Ocean showed that upwelling controls the salinity anomalies whenever the vertical salinity stratification of seawater is not so weak [36]. Evaporation transfers energy to the atmosphere as latent heat. This action not only cools the upper ocean but also salinizes the ocean mixed layer [43]. In contrast, precipitation can cause a drop in surface salinity [18,24,27]. During the approach of Typhoon Choi-Wan (2009), a freshening signature in the MLS due to intense

rainfall was observed at a mooring located in the Kuroshio Extension area [27]. Another study which analyzed the underwater glider data found that typhoons, accompanied by heavy rainfall, can cause subsurface layer freshening [44]. A series of numerical simulations showed that the desalination rate due to precipitation can exceed the salination rate due to the entrainment of high-salinity water from below, resulting in a salinity decrease in the mixed layer rather than an increase [45].

In situ observation data is an important basis of scientific research. A cross-shaped observational array was deployed in the South China Sea (hereafter SCS) to capture information about the TC-induced upper ocean response [4]. Fortunately, Typhoon Kalmaegi (2014) passed over this array in September 2014, and the variation of atmospheric conditions and oceanic thermal conditions induced by Kalmaegi (2014) were both documented by this array. Based on this in situ observations and other datasets, the upper ocean thermodynamic and dynamic responses to Typhoon Kalmaegi had been investigated in [3,4,46]. It was found that the maximum cooling of SST reached 6 °C, which was mainly induced by vertical mixing and upwelling [3]. The dynamic response was studied in [4], which indicated that the effect of upwelling in the subsurface layer was comparable to vertical mixing, and the cold suction effect need to be taken seriously. Furthermore, the net modulation mechanism of upper ocean temperature variations caused by Typhoon Kalmaegi was studied in [46]. Different from the three studies, this study focus on the role of precipitation on the TC-induced upper ocean salinity response rather than the thermal response induced by Kalmaegi.

The main goal of this paper is to investigate the influence of TC precipitation on TC-induced upper ocean response. The simultaneous precipitation and salinity data provided by in situ observations can help us understand the relationship between these two elements. The infrared (IR) satellite cloud images and satellite-based retrieval of precipitation provide us with consistent and reliable data over an open ocean, which help us to investigate the evolution of TC's structure and precipitation distribution. Moreover, the possible influence of typhoon precipitation on the upper ocean temperature and salinity responses is investigated via a three-dimensional oceanic numerical model. In summary, this study is based on satellite observations, in situ observations, and a numerical model to reveal the air-sea responses, precipitation characteristics, and the effect of precipitation on ocean responses during Typhoon Kalmaegi (2014).

The data and numerical model in use are introduced in Section 2. The results are showed in Section 3, which includes the observed atmospheric features, the corresponding ocean responses, and the influence of precipitation on ocean responses. Section 4 presents the discussions of this work.

2. Data and Methodology

2.1. TC Data

The TC track are provided by the China Meteorological Administration (CMA) best track dataset [47,48]. The CMA best track dataset contains information on all identified TCs since 1949, including tropical depression cases. This dataset emphasizes TCs that were close to China [49,50]. Figure 1 shows the lifetime of Typhoon Kalmaegi. The storm was formed on the ocean east of Philippines at 18:00 UTC on 10 September 2014, then grew to a typhoon at 00:00 UTC on 14 September with the maximum sustained wind (MSW) of 35 m/s. After passing through the Philippines, it weakened by 2–3 m/s. Then it intensified again because of the abundant energy and water vapor supply from the warm SCS, reaching its peak at approximately 18:00 UTC on 15 September and was maintained for 12 h with minimum sea level pressure (MSLP) of 960 hPa and MSW of 42 m/s. Then, Kalmaegi moved northwestward and eventually decayed in Vietnam. The average translation speed when Kalmaegi rapidly passed through the observational array was approximately 8.5 m/s during 14–16 September.
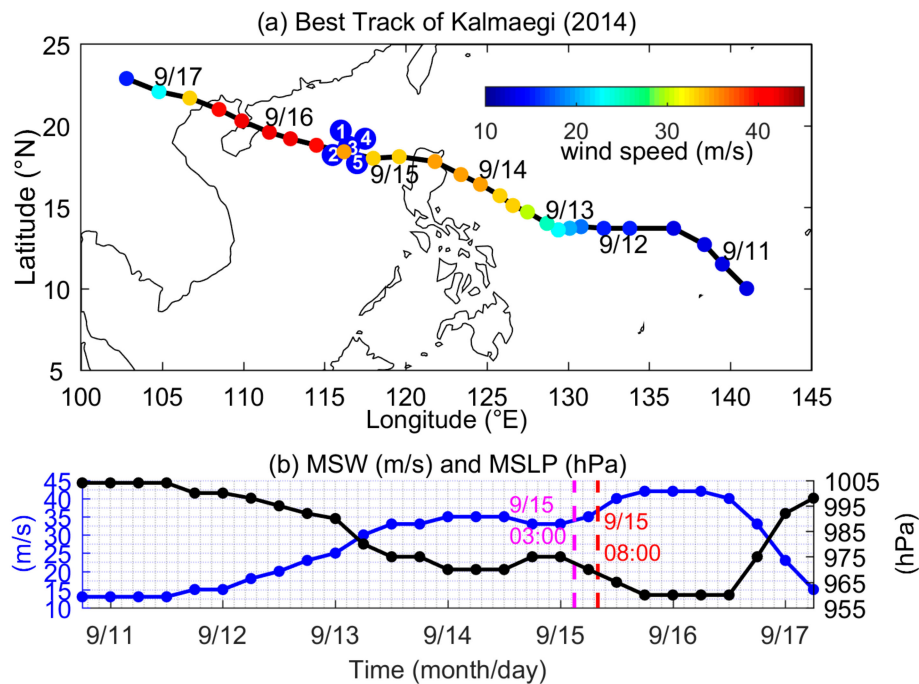
Figure 1. (**a**) Track of Kalmaegi (2014) from the CMA. Blue dots with white numbers (1–5) showed the buoy positions. The color bar shows the value of MSW (m/s), which indicates the intensity. (**b**) MSW (m/s, blue line) and MSLP (hPa, black line) of Kalmaegi (2014) from the CMA best track dataset. The magenta vertical line and red vertical line represent the time when the typhoon center reaches those stations, which are UTC 03:00 on 15 September (Stations 4 and 5) and UTC 08:00 on 15 September (Station 2), respectively.

2.2. Satellite Data

We used satellite IR cloud imagery to study the typhoon structure and cloud system. The IR cloud images are derived from the cloud-top black body temperature (TBB) of the Japanese Multi-functional Transport Satellite (MTSAT) observations. The MTSAT-1R (140° nadir position) provided satellite imagery from 28 June 2005 to 30 June 2010 and was then converted to an on-orbit standby satellite. The MTSAT-2 (145° nadir position) assumed the observational task of MTSAT-1R from 1 July 2010 to 4 December 2015. Each satellite has five wavelength bands, including four infrared channels and one visible channel [51]. The IR1 channel (from 10.3 μm to 11.3 μm), which detects surface or cloud-top temperature, was used in this study. The data was distributed on a 0.05° × 0.05° grid with a time interval of one hour and can be downloaded from the website of Kochi University, Japan [52,53].

We also used the National Oceanic and Atmospheric Administration (NOAA) Climate Prediction Center Morphing Technique (CMORPH) dataset to study the rainfall pattern during the passage of Typhoon Kalmaegi through our observational array [54]. The CMORPH dataset precipitation is estimated from low-orbiter satellite passive microwave observations, as well as the geostationary satellite IR data during periods when instantaneous passive microwave data were not available [55]. The CMORPH dataset incorporated four other satellite precipitation data derived from passive microwave observations [55,56]. The data used here was provided with 0.25° resolution on a 3-h time interval. Although the CMORPH data is a grid average which may underestimate the maximum of precipitation, it is one of the few precipitation data available on the open ocean. To obtain more accurate simulation results, the CMORPH data were interpolated to a model-suitable grid as the boundary condition (freshwater flux) in the numerical simulations.

2.3. In Situ Observations

An observational array in the SCS captured information about the passage of Typhoon Kalmaegi. This array consists of five stations, including subsurface moorings and moored buoys. Locations of five stations were showed in Figure 1. The track data from CMA showed that Typhoon Kalmaegi passed approximately 40 km and 32 km (142 km) to the north (south) of the Stations 2 and 5 (Station 4). The ocean salinity and temperature profiles were measured every 2 min by conductivity temperature depth (CTD) sensors. The meteorological variables were measured at 4 m above the ocean. The time intervals were 1 h at Stations 4 and 5 and 12 min at Station 2. Note that several CTD recorders at Station 1 were lost, and the buoy at Station 3 floated away due to the broken wire rope, so we did not analyze the data at Stations 1 and 3 in this work. To match the salinity and temperature observations, only the data from Stations 2, 4, and 5 are analyzed in this study. More details of the observational array and the observational data, such as the longitude, latitude, water depth, and instruments of each station, can be seen in [4].

2.4. The Numerical Simulation Setups

The numerical model used is a three-dimensional version of the Price–Weller–Pinkel model (3DPWP) [57]. A delicate part of 3DPWP is about the parameterization scheme of sub-grid vertical mixing. In 3DPWP, vertical mixing happens when any of the three instability conditions are satisfied. The three instability criteria are static instability, mixed layer instability, and shear flow instability, and the corresponding mixing processes are free convection, mixed-layer entrainment, and gradient mixing, respectively [57].

Previous studies have proved that this model can well simulate the physical processes that occur in the TC-induced ocean response [58,59]. The study of using 3DPWP to simulate the upper ocean response caused by Typhoon Kalmaegi had also yielded reliable results [4]. It is shown that the model settings used in [4] can generally reconstruct the wind forcing field of Kalmaegi and the corresponding upper ocean responses. By comparing the deviation between the observed wind at our observational stations and the simulated wind field of three ideal models, the Sea, Lake and Overland Surge from Hurricanes (SLOSH) method was selected to construct the high-resolution wind field for the model (see Appendix A,B in [4] for details). As for the surface heat flux, there are no reasonable ways to estimate a large range of heat flux field based on meteorological observations at several points during a typhoon. In addition, previous studies have also shown that the surface heat flux caused only 10%–30% of the nonreversible heat exchange into the mixed layer, while entrainment caused the rest [2,4]. It is clear that the air-sea heat exchange is less important to the heat budget in the mixed layer than entrainment. Thus the air-sea heat flux was not considered in the model boundary conditions. Since the typhoon case in this study is also the Typhoon Kalmaegi, the same model settings including the ocean initial conditions as in [4] is applied in this study. The basic model settings of the two studies differ only in the model range and resolution.

To explore the importance of precipitation to the upper ocean responses during a typhoon, we conducted two numerical experiments by controlling the presence or absence of precipitation forcing, which were referred to as experiments 'Pre' and 'Nopre', respectively. Table 1 lists the set of performed numerical experiments. The ocean initial conditions and model configuration are the same as in [4], except for the model range and resolution. In the model, Stations 2, 4, and 5 are represented by the corresponding locations of x = −40 km, x = 144 km, and x = −32 km, respectively, noting that the positive (negative) value means the right (left) side of Kalmaegi's track. After being interpolated to the model grid, the CMORPH precipitation at a 3-h time interval was injected into the ocean model every 3 h. The precipitation was injected into the first layer of the model and then gradually penetrated downward under the effect of dynamic processes. The only difference between experiments Nopre and Pre was the surface precipitation, so we can regard the discrepancy in the oceanic responses between experiment Nopre and Pre as the effect of precipitation.

Table 1. Details of numerical experiments.

Configuration	
Vertical layers	160
Vertical resolution	10 m
Horizontal resolution	16 km
Horizontal grids	151 (across-track) × 801 (along-track)
Domain size	2400 km (across-track) × 12,800 km (along-track)
Time interval	120 s
Boundary condition	Radiation boundary condition
Wind field of TC	SLOSH method [60]
Coriolis parameter	4.876×10^{-3} (at 18.7° N, the latitude of Station 3)
Inertial period	37.33 h
Drag coefficient (Cd)	$Cd \times 10^3 = 1.2$, W ≤ 11 m/s; $= 0.49 + 0.065$ W, $11 < W ≤ 19$ m/s; $= 1.364 + 0.0234$ W $- 0.0002$ W^2, $19 < W ≤ 100$ m/s [61]
Surface heat fluxes	Not included
Surface freshwater flux	Include for 'Pre' simulation and exclude for 'Nopre' simulation

3. Results

3.1. The Atmospheric Evolution Results

The IR satellite cloud images and horizontal distribution of CMORPH precipitation at six important times of the 14–16 September are shown in Figures 2 and 3. When traveling through our observational array, the convective system was asymmetric, with more (less) convection located on the left (right) of the track. This asymmetry is likely associated with the active southwest monsoon over the SCS, which transports moist and warm airflow and promotes the convergence of wet and unstable air in the TC outer circulation when the monsoon connected to the TC outer circulation [62,63]. The land on the north side of Kalmaegi also attributed to this asymmetry due to the large surface friction and poor water vapor condition above land. A detailed look at the cloud system over the three stations shows that the low-pressure center of Kalmaegi approached Stations 4 and 5 at 00:00 UTC on 15 September (Figure 2c) and then approached Station 2 approximately 6 h later (Figure 2d). Stations 4 and 5 were affected by the central dense overcast (CDO) during this period, and Station 2 was influenced by CDO from 06:00 UTC on 15 September to 09:00 UTC on 15 September. Thereafter, as Kalmaegi continued to intensify and moved away, the observational array was mostly affected by clouds in the rear of the outer spiral rainband (Figure 2e). By 00:00 UTC on 16 September (Figure 2f), Kalmaegi moved to the east side of Hainan Island and then made landfall. Clearly, all stations are mainly affected by scattered clouds that are far from the primary vortex.

In Figure 3, the positions of the heavy precipitation center were consistent with the low TBB area in the spiral rainband and CDO area. As Kalmaegi gradually intensified, the spiral rainbands were established and connected to the inner-core region. The precipitation cell was first concentrated in the CDO area (Figure 3a,b) and then extended to a wider range containing the CDO area and spiral rainband (Figure 3c–f). Moreover, CMORPH precipitation and cloud patterns share a similar asymmetry, with heavy rainfall centers and more convective clouds located on the south side of the whole cloud system. Both the southwest monsoon and topography contribute to the asymmetric rainfall distribution, resulting in more convective precipitation in the left quadrant [64,65].
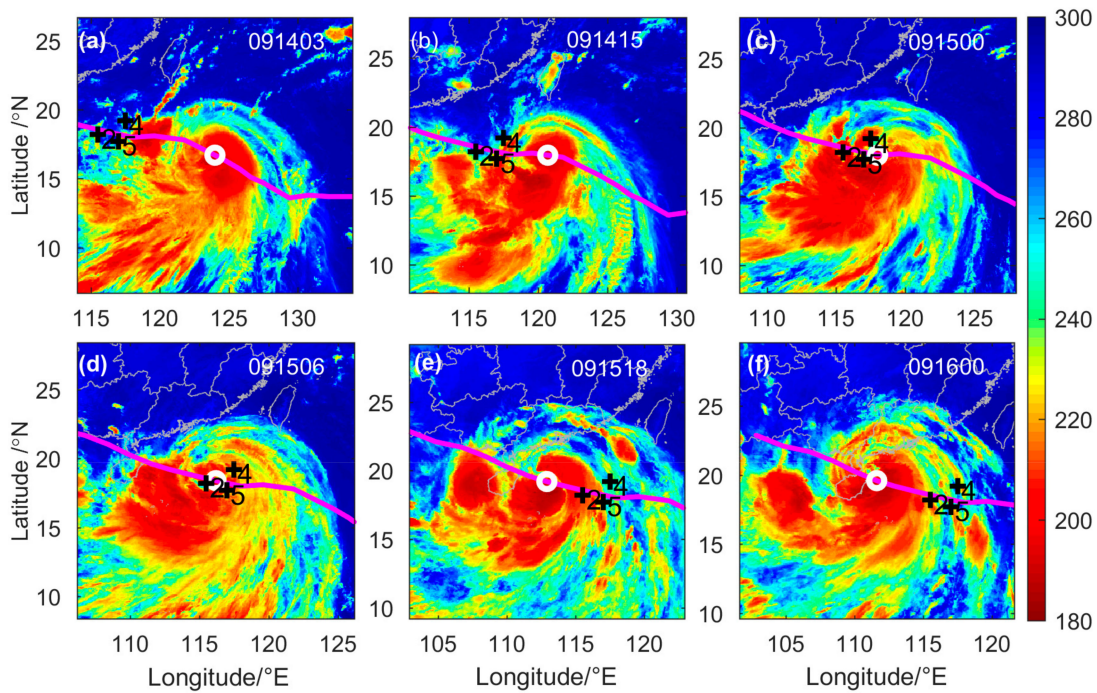
Figure 2. MTSAT-2 satellite cloud-top TBB (K) images at 6 different times: (**a**) 03:00 UTC on 14 September; (**b**) 15:00 UTC on 14 September; (**c**) 00:00 UTC on 15 September; (**d**) 06:00 UTC on 15 September; (**e**) 18:00 UTC on 15 September; (**f**) and 00:00 UTC on 16 September. The pink solid lines denote the track of Kalmaegi, and the white rings denote the location of the TC center. Black plus signs with numbers indicate the positions of Stations 2, 4, and 5. The time is marked at the top right of each picture.
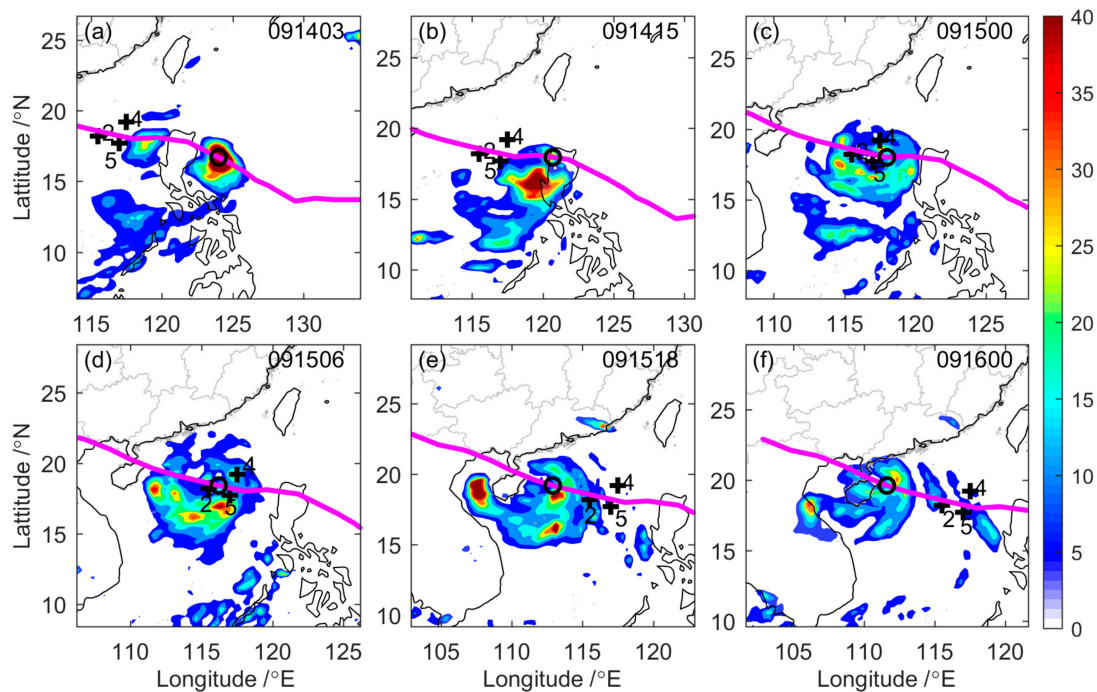
Figure 3. CMORPH precipitation (mm/3 h) distribution at 6 different times: (**a**) 03:00 UTC on 14 September; (**b**) 15:00 UTC on 14 September; (**c**) 00:00 UTC on 15 September; (**d**) 06:00 UTC on 15 September; (**e**) 18:00 UTC on 15 September; (**f**) and 00:00 UTC on 16 September. The pink solid lines denote the storm track, and the black rings denote the location of the TC center. Black plus signs with numbers indicate the positions of Stations 2, 4, and 5. The time is marked at the top right of each picture.

The precipitation at Station 4 appeared at 03:00 UTC on 14 September, then reached the peak at approximately 41 mm/h at 21:00 UTC on 14 September with a total duration of approximately 54 h (Figure 4b). The precipitation at Station 5 began at approximately 05:00 UTC on 14 September and then reached a maximum of 133 mm/h at 06:00 UTC on 15 September (Figure 4c). There were four rainfall processes at Station 5, and each stage experienced a different precipitation system. The first period (from 05:00 on 14 September to 13:00 on 14 September) was mainly induced by the convective cloud cluster on the east side of Station 5 (Figure 2a), while the second process (15:00 on 14 September to 00:00 UTC on 15 September) was induced by the CDO cloud (Figure 2b). The center area passed over Station 5 at approximately 02:00 UTC on 15 September; thus, the third process (from 04:00 on 15 September to 13:00 on 15 September) may be induced by the intense convection in the eyewall. The fourth stage of precipitation (from 14:00 on 15 September to 00:00 on 16 September) was the weakest and was likely generated by the scattered clouds in the distant rainbands (Figure 2f). As for Station 2, the precipitation appeared at 21:00 UTC on 14 September and reached a maximum of approximately 33.4 mm/h at 00:00 UTC on 15 September, when it was being affected by a spiral rainband (Figures 2c and 3c). It should be noted that the precipitation at Station 5 is stronger than that at Station 4. This cross-track difference is probably related to the asymmetric TC rainfall distribution (Figure 3).
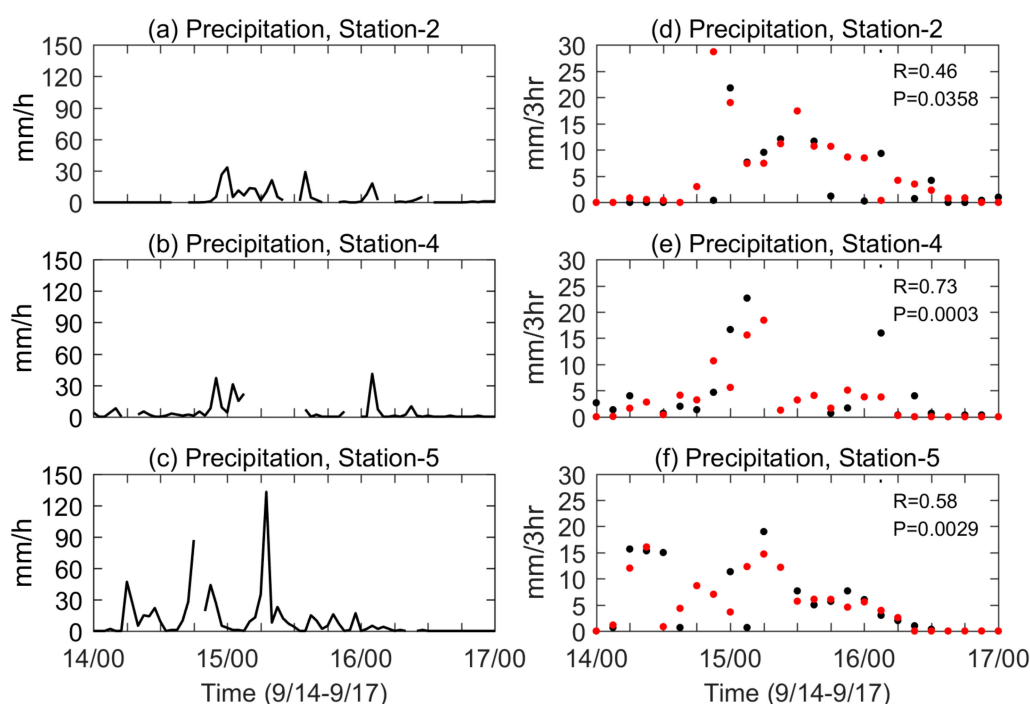
Figure 4. (**a–c**) Hourly precipitation from the observation array at three stations during 14–17 September. (**d–f**) Three-hourly precipitation from the observational array after an average of 3 h (black dots) and three-hourly CMORPH rainfall (red dots) at three stations during 14–17 September. The three rows from top to bottom represent the data at Stations 2, 4 and 5, respectively. The R and *P* values in (d-f) represent the correlation coefficients and the corresponding significance level between the CMORPH data and measured precipitation. After excluding the CMORPH data at the time when there was no available data of observed precipitation, the two datasets used to calculate the correlation have the same sample number, which were 21 (Station 2), 19 (Station 4), and 24 (Station 5), respectively. Note that these samples correspond one-to-one in time.

As shown in Figure 4d–f, the correlation coefficients between CMORPH data and the measured precipitation at the three stations are 0.46, 0.73, and 0.58 respectively. The corresponding *p* values (i.e., significance level) are 0.0358, 0.0003, and 0.0029, respectively. Generally, a *p* value of less than 0.05 means that the correlation between the two datasets is significant. The correlation coefficients at Stations 4 and 5 were both larger than 0.5 and the *p* values at the three stations were all less

than 0.05, indicating that these correlations were all significant. Therefore, the CMORPH data were consistent with the observed precipitation (Figure 4d–f), we can use it as the freshwater forcing in the numerical model.

Figure 5 shows the temporal evolution of basic meteorological elements at Stations 2, 4, and 5 from 14 to 17 September. The double-peak wind speed curves and V-shaped structure air pressure curves of all three stations indicate that they were close to the typhoon eye (Figure 5d–f). These two peaks occurred when the western and eastern sides of the eyewall passed over these stations, and the minimum values of the wind and air pressure correspond to the time when the central eye was closest to them (approximately 08:00 UTC (03:00 UTC) on 15 September for Station 2 (Station 5)). The change in the wind direction also illustrates this characteristic (Figure 5g–i). The wind vectors at Stations 2 and 5 (Station 4) rotated anticlockwise (clockwise) with time because Kalmaegi passed to the north (south) of Stations 2 and 5 (Station 4). When it approached these stations, the air temperature decreased and the relative humidity increased (Figure 5a–c). The typhoon eye is well-known to be the vortex center of high temperature, dry air, weak wind, and even static wind [66]. From 06:00 UTC to 10:00 UTC on 15 September (20:00 UTC on 14 September to 03:00 UTC on 15 September), the temperature at Station 2 (Station 5) increased rapidly as the eye passed. The temperature decreased to lower than before in the following several hours, indicating that the eyewall on the east side was weaker than that on the west side. Moreover, it should be noted that at three stations, the surface wind reproduced by the SLOSH method in the model is consistent with the measured wind [4].
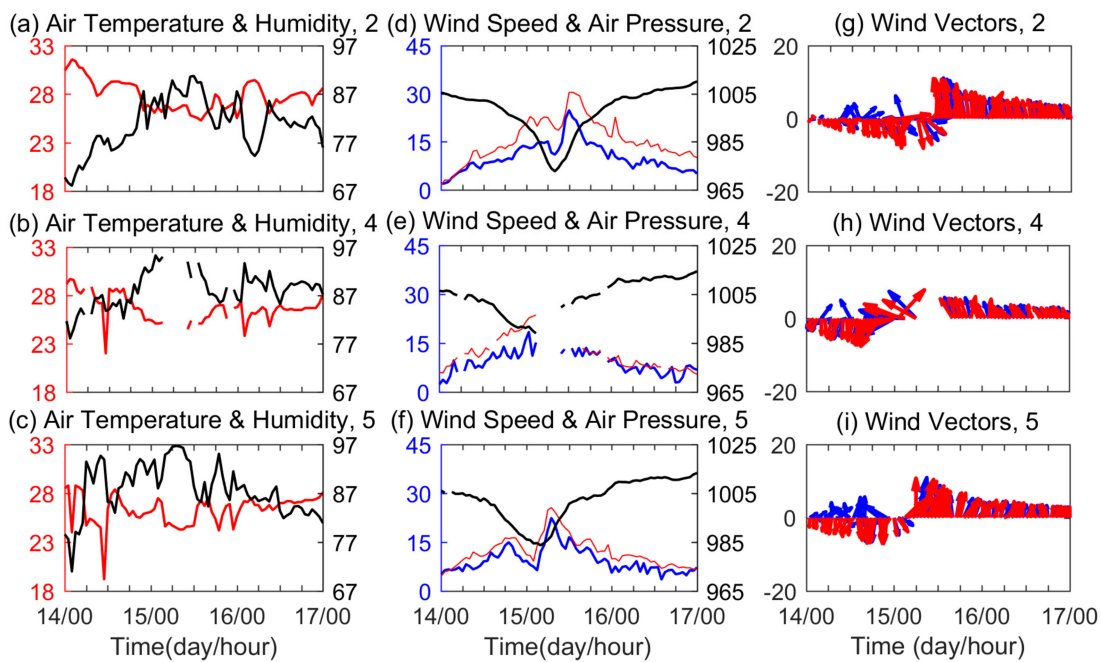
Figure 5. Time series of (**a–c**) air temperature (°C, red line) and relative humidity (%, black line), (**d–f**) 2-min sustained wind speed (m/s, blue line), 2-min gust wind speed (m/s, red line) and central pressure (hPa, black line), and (**g–i**) wind (blue) and wind gust (red) vectors observed at Stations 2, 4, and 5. Upward (rightward) arrows indicate northward (eastward). The three rows from top to bottom represent the data at Stations 2, 4, and 5, respectively.

3.2. Observed Salinity Responses

The ocean temperature variations during Typhoon Kalmaegi at Stations 2, 4, and 5 had been discussed in [4], thus, we mainly focus on salinity response in this paper. The measured and model simulated salinity responses at three stations are plotted in Figure 6. After Kalmaegi, the MLS anomaly at Station 4 was always positive, and the maximum surface positive anomaly was 0.176 psu (Figure 6b). In contrast, the anomalies at Station 5 showed a pronounced freshening tendency

(Figure 6c), with a maximum SSS decrease (increase) of 0.278 psu (0.103 psu). For Station 2, the MLS experienced an obvious desalination process at first (from 10:00 UTC on 15 September to 02:00 UTC on 16 September) and was then dominated by an increasing tendency (Figure 6a). The largest negative (positive) anomaly of SSS at Station 2 was approximately −0.145 psu (0.155 psu). The intense vertical mixing during Kalmaegi contributed to the SSS increase. However, the temporary desalination process was probably related to intermittent precipitation because it can inject freshwater into ocean and decrease SSS [18,24,27,44]. As the MLS had different response features at these stations, it is uncertain whether salinity has the same rightward-bias feature as SST cooling, which reflects that the effects of other processes on the MLS besides the vertical mixing were not negligible. In the subsurface layer, there is fresh anomalies alternated with the salty anomalies at all three stations, which coincided with the near-inertial pumping. Moreover, a fresh (salty) anomaly dominated the salinity anomalies at Station 4 (Stations 2 and 5). A cross-track difference in the tendency of salinity response both existed in the surface layer and subsurface layer, but the causes of the differences in these two layers were quite different. In the mixed layer, is due to the difference in the coupling strength of the current velocity and the clockwise-rotated inertial current as well as the asymmetry of precipitation while, in the subsurface layer, the difference arises from different dominant dynamic mechanisms on both sides of Kalmaegi's track [46]. That is, upwelling increases the subsurface salinity, which is the dominant mechanism at Stations 2 and 5; while vertical mixing decreases the subsurface salinity, which is the dominant mechanism at Station 4.
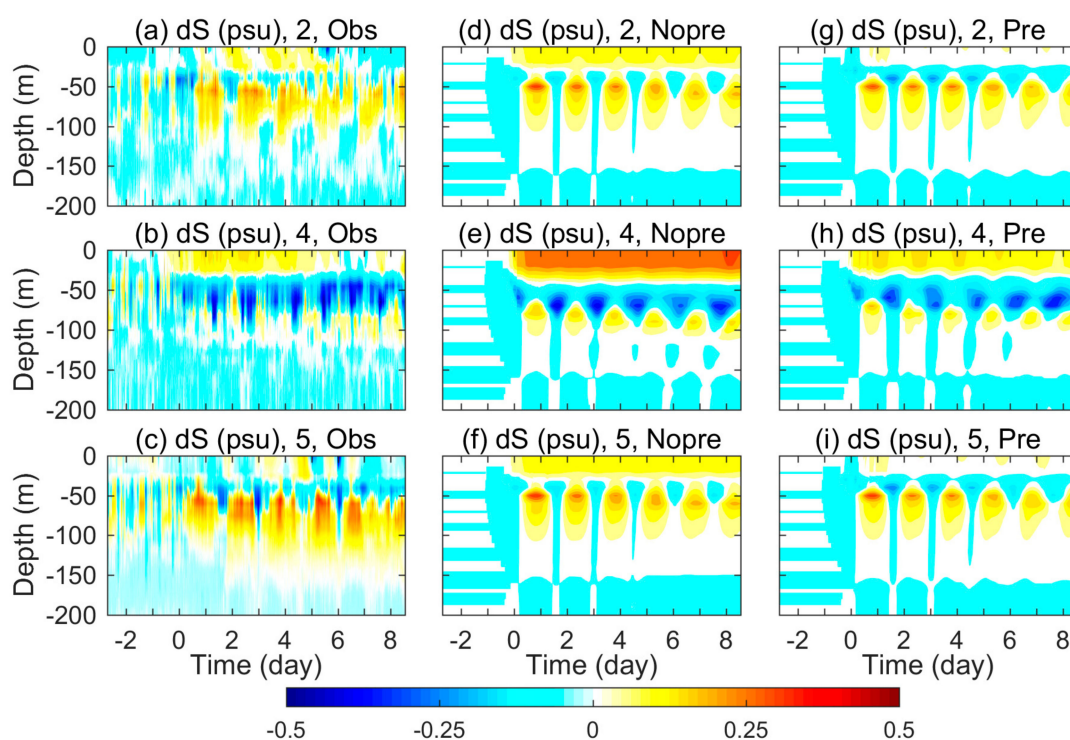
Figure 6. Salinity anomalies obtained from observations, Nopre and Pre simulations at Stations 2 (**a–c**), 4 (**d–f**), and 5 (**g–i**). The 0 on the x-axis represents the arrival time of Kalmaegi. The top X-axis in (**a,d,g**) show the actual date (month/day). The three rows from top to bottom represent the data obtained from observations, Nopre and Pre simulations, respectively.

Since our model settings are similar to [4], and the simulation effect and temperature response had been examined in [4], we will analyze the model results directly without model validation. To be honest, the simulation results of salinity were unsatisfactory, especially of the MLS. In experiment Nopre, the simulated MLS anomaly was always positive and increased more than the observations (Figure 6b,e,h). The decrease in MLS in the observations at Stations 2 and 5 (Figure 6a,g) were difficult

to simulate (Figure 6b,h). However, the evolution of the anomaly of MLS at all stations was closer to the observations when precipitation was considered (Figure 6c,f,i), and the overestimation of the MLS increase in experiment Nopre was effectively suppressed. Regarding the subsurface response, the oscillation in the model was more periodic, which probably arose from the lack of non-typhoon signals in the observed background field, such as the diurnal tides and ocean eddies [67,68].

3.3. Precipitation Effects on Ocean Temperature and Salinity

In this section, we will carefully analyze the relationship between precipitation and salinity during Kalmaegi. Combining Figures 4 and 6, we found that during the main precipitation stage (from 14 September to 17 September), several salinity desalination processes occurred (Figure 6) at Stations 2 and 5, which had good consistency with the precipitation intensity and period (Figure 4). At Station 2, when precipitation reached its peak (35 mm/h) at 00:00 UTC on 15 September, the near-surface layer salinity (up to 22.5 m) was immediately diluted. Then, freshening occurred only within 10 m depth below the sea surface. Simultaneously, the precipitation was relatively weak, and the vertical mixing was probably inhibited by stable stratification caused by previous precipitation. A more significant desalination process occurred from 10:00 UTC on 15 September to 02:00 UTC on 16 September. As the precipitation accumulated, the seawater within the 15 m surface layer was diluted. This low-salinity water mass penetrated downward gradually over time and reached the bottom of the mixed layer (approximately 30 m) via entrainment and downwelling. Note that the negative SSS anomaly disappeared at approximately 22:00 UTC on 15 September, while the negative anomaly at the bottom of the mixed layer persisted until 02:00 UTC on 16 September. The time lag indicates that the precipitation freshwater can spread downward into deeper oceans. There were also salinity dilution processes at Station 5. After the first stage of rainfall (05:00 UTC on 14 September to 13:00 UTC on 14 September), the SSS decreased, and the freshwater immediately reached a depth of 17.5 m. The rainfall resumed after 2 h. Subsequently, the MLS (approximately 22.5 m depth) at Station 5 became fresher since 19:00 UTC on 14 September, which may be attributed to the continuous and intense rainfall. Long-lasting precipitation could bring large amounts of freshwater into the local mixed layer and directly reduce the salinity. The negative SSS anomaly implied a stronger effect of precipitation than the effect of vertical mixing and upwelling at Stations 2 and 5. In other words, the surface salinity reduction at Stations 2 and 5 are closely related to the precipitation of Kalmaegi.

The temperature difference and salinity difference between experiments Pre and Nopre are presented in Figure 7. Here, we choose data from the arrival time to 1.5 days after Kalmaegi represent the 'forced stage' [11]. The obvious positive temperature difference and negative salinity difference above 50 m depth indicates that the effect of precipitation in the 3DPWP model will weaken the salinity increase and temperature cooling in the surface layer. Note that the salinity reduction occurred at both sides of the track, while the temperature increase mainly occurred at the right side of the track. At Station 4, the temperature change caused by precipitation was approximately 6 times than that of the other two stations. After the forcing stage, the maximum warm (fresh) difference in SST (SSS) reached approximately 0.19 °C, 1.12 °C and 0.23 °C (−0.16 psu, −0.30 psu, and −0.17 psu) at the three stations (2, 4, and 5). In the subsurface layer, the differences were alternate negative and positive at Stations 2 and 5, while the differences at Station 4 were dominated by significant cooling in temperature and increase in salinity. Under the effect of precipitation, the mixed layer temperature cooling and salinity increasing are directly reduced by the reduction in vertical mixing. The freshening of MLS due to precipitation strengthens the stratification and then inhibits vertical mixing and vertical advection.

The ratio of SST and SSS difference between Pre and Nopre to the corresponding anomalies in experiment Nopre are plotted in Figure 7d,h. The ratio in the forced stage varied greatly because of the strong vertical mixing caused by the wind stress forcing. Within 7 days after the forced stage, the SST cooling (SSS increasing) at the three stations in experiment Pre was approximately 3.8%, 15.1%, and 2.7% (63.6%, 52.6%, and 63.0%) weaker than that in Nopre, with a mean difference in temperature (salinity) of approximately 0.039 °C, 0.40 °C, and 0.032 °C (−0.074 psu, −0.152 psu, and −0.078 psu)

respectively (Figure 7). These discrepancies were also rightward biased, with stronger SST warming and SSS decreasing induced by precipitation appeared on the right side (Station 4). Although the salinity difference was largest at Station 4, it had the smallest ratio. This is because the violent vertical mixing on the right side produced a large salinity anomaly, so the influence of precipitation was relatively small. Moreover, the smaller ratio of temperature than salinity indicates a stronger salinity response to precipitation than temperature.
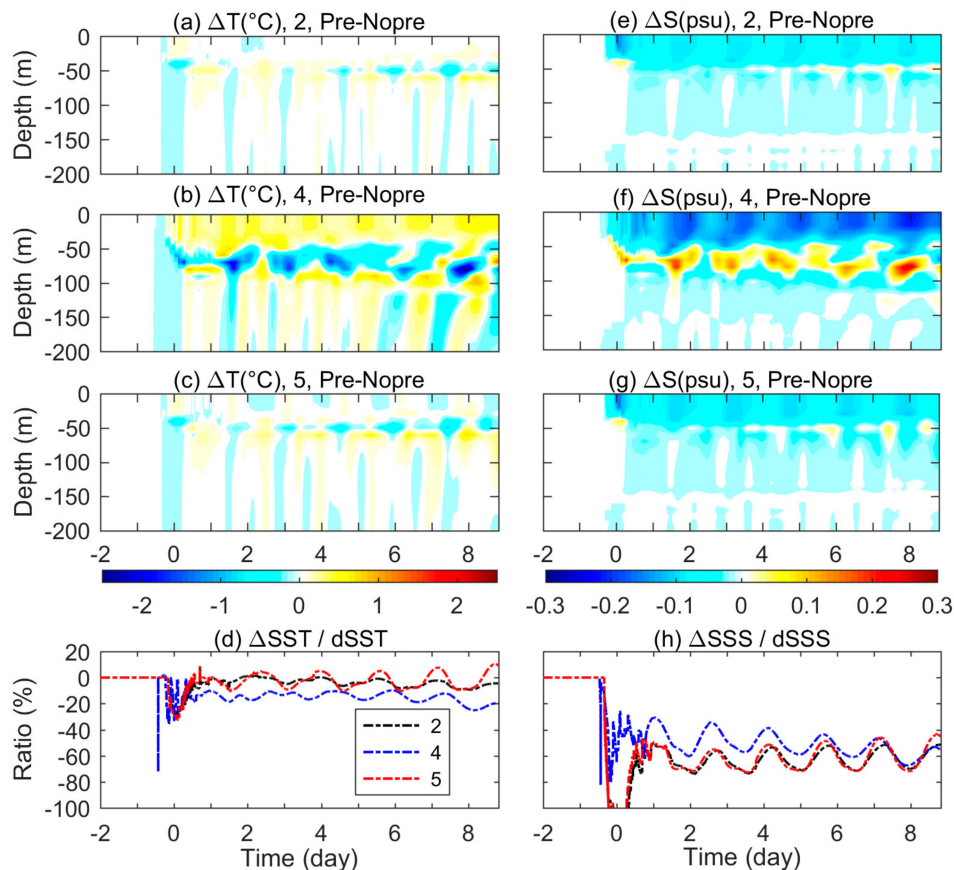
Figure 7. The discrepancies in (**a**–**c**) temperature (ΔT, °C) and (**e**–**g**) salinity (ΔS, psu) above 200 m between the Pre and Nopre cases at three stations. The values were calculated using Pre minus Nopre. (**d**) The ratio of the SST difference between Pre and Nopre to SST anomaly in Nopre, and (**h**) same as in (**d**) but for SSS. The 0 on the x-axis represents Kalmaegi's arrival time. The first three rows from top to bottom represent the data at Stations 2, 4, and 5, respectively.

Induced by Kalmaegi, the salinity profiles exhibited a three-layer "salty-fresh-salty" vertical structure at Stations 4 (Figure 8b). Unlike Station 4, the fresh layer at Station 2 was so thin and weak that the salinity at Station 2 showed an overall increasing structure. The SSS increased by 0.015 psu and 0.088 psu at Stations 2 and 4, respectively, while the SSS decreased by approximately 0.007 psu at Station 5 (Figure 8c). At Station 5, a freshened layer occurred in the 10 m surface layer and was most likely attributed to the intense precipitation of Kalmaegi. However, it may also be a false signal due to observational errors. Except for the decrease in surface salinity at Station 5, the salinity in deep layer showed fresh-salty vertical structures. The vertical salinity structure in both model results showed a same salty-fresh-salty vertical structure at all three stations, although the deeper salty layer was less clear than the shallow one. In the Nopre experiment, the fresh layer appears in the depth range between 25 m and 45 m, 35 m and 85 m, 25 m, and 50 m at Stations 2, 4, and 5, respectively, while the fresh layer in Pre appeared at a shallower depth (approximately 20 m, 25 m, and 20 m at Stations 2, 4, and 5, respectively) and ended at the same depth as that of Nopre. The overestimation of SSS increase in Nopre was greatly weakened by precipitation, and the layer of salinity increase became

shallower under the effect of precipitation. On one hand, precipitation can cause a rapid decreases of salinity in a thin layer on the sea surface, the fresh water then penetrate downward through vertical mixing, resulting in a weaker increase in MLS and a stronger salinity decrease at the top of thermocline layer. This is the direct dilution effect of precipitation. On the other hand, freshened mixed layer strengthened vertical stratification, inhibits the vertical mixing, results in a mixed layer shallower than the case without precipitation. This is the indirect effect of precipitation. The SST cooling at Station 4 was 0.37 °C lower in Pre than that in Nopre, and the warming in subsurface layer was also weaker than that of Nopre, which makes the simulation closer to the observations. The effect of precipitation at the left side of the track was not significant, as seen from nearly overlapped post-storm temperature profiles of Nopre and Pre in Figure 8d,f. It is clear that the precipitation has a more obvious effect on salinity than on temperature.
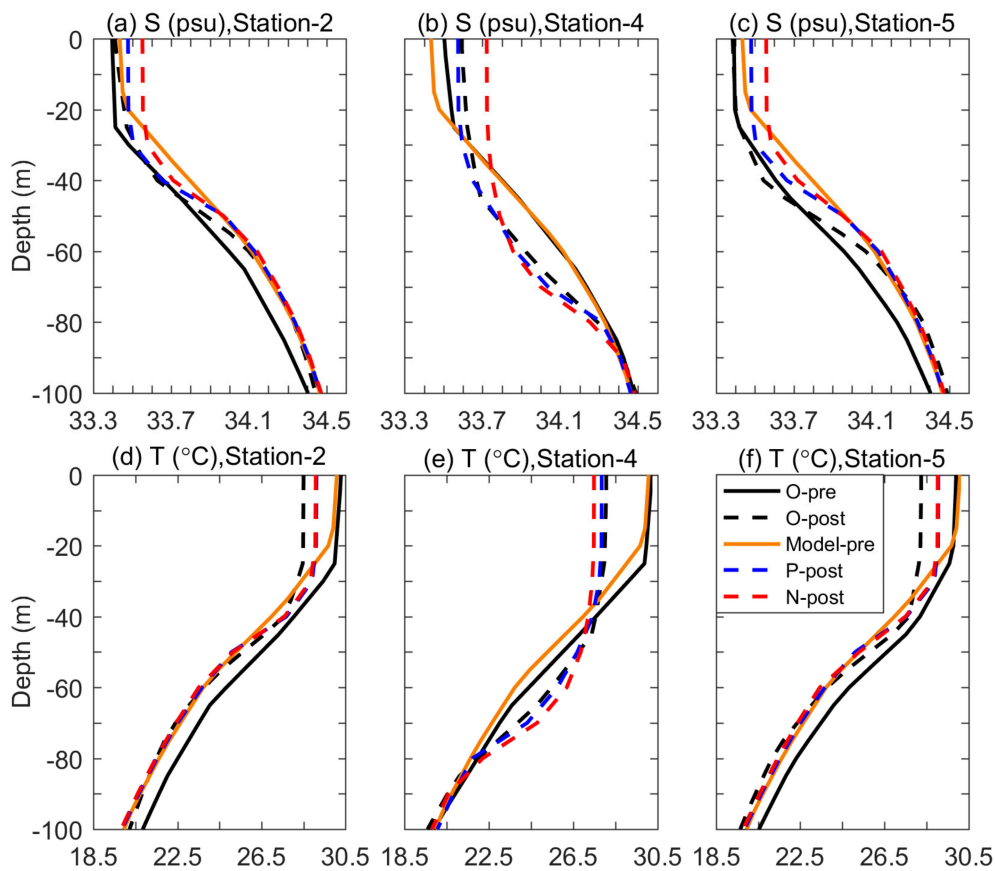
Figure 8. Average profiles of (**a–c**) salinity and (**d–f**) temperature above 100 m before and after Kalmaegi at Stations 2, 4, and 5. The solid lines represent the pre-storm value calculated by the average during 10 September to 14 September. The dotted lines represent the post-storm value, which is the average of the second to fifth inertial periods after the storm. Note that two model simulations share the same initial conditions, i.e., pre-storm vertical profiles, which are represented by a yellow solid line. Black lines, blue lines, and red lines represent the values in the observations and Pre and Nopre cases, respectively.

3.4. Precipitation Effects Reflected by Dynamic Processes

In 3DPWP model, horizontal advection, vertical advection and vertical mixing are three crucial processes that modulate the ocean thermohaline condition. Figures 9 and 10 show the model simulated post-storm average temperature anomaly and salinity anomaly caused by these three terms respectively. The minus (plus) sign is to the left (right) side of the track.
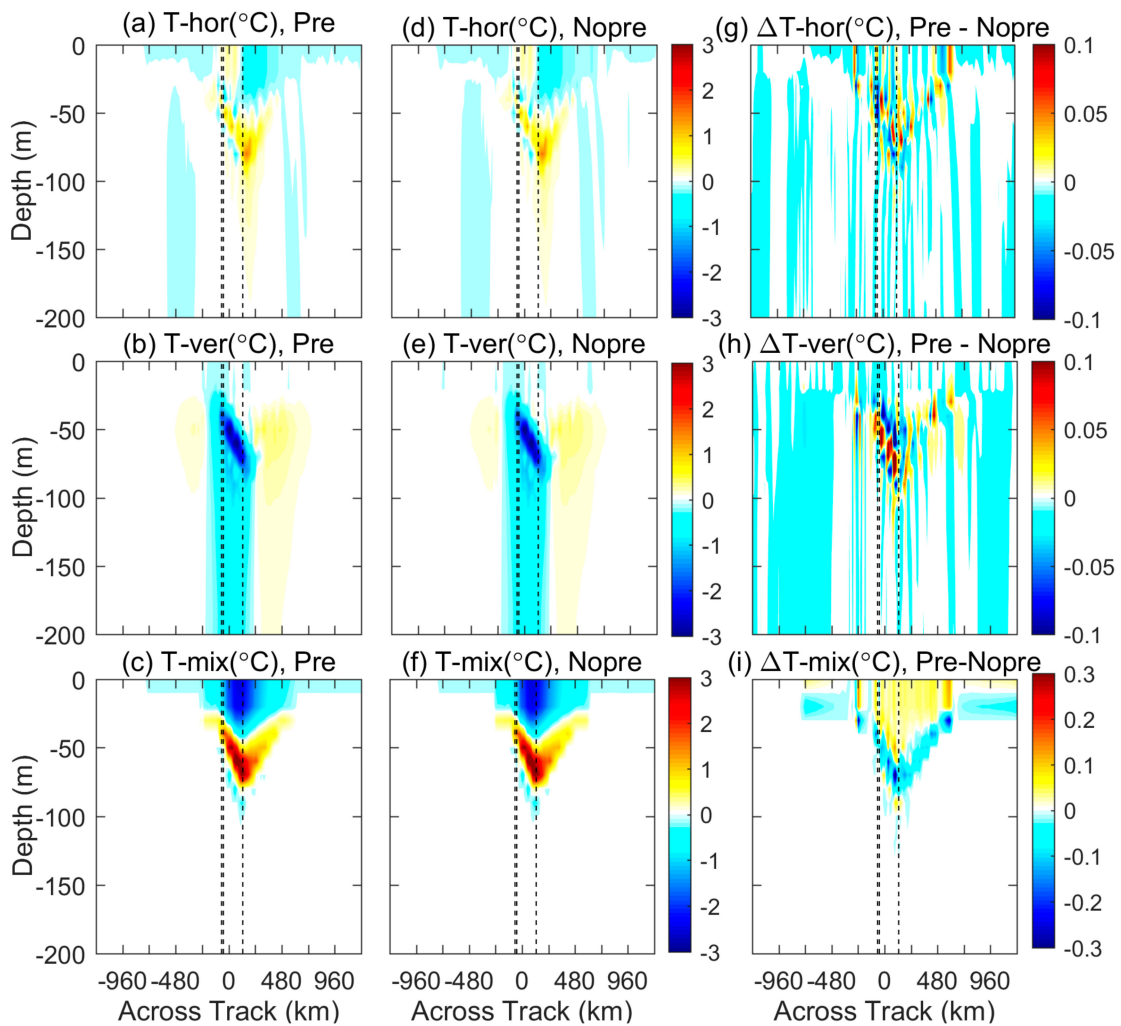
Figure 9. Post-storm average temperature induced by horizontal advection, vertical advection, and vertical mixing in experiment (**a–c**) Pre, (**d–f**) Nopre, and (**g–i**) the corresponding differences between Pre and Nopre. The average is taken for the second to fifth inertial periods after the storm. Note that there are two dotted lines to the left of the track, representing the positions of Stations 2 and 5. The dotted line at the right side represent the locations of Station 4.

The horizontal advection is the weakest one among the three dynamic processes. In the surface 50 m layer, warm advection occurred near the track and cold advection happened in the outward region, accompanied by a thick layer of warm advection occurred in the subsurface layer (50–100 m) (Figure 9a,d). The obvious difference between Pre and Nopre is a V-shaped band consisting of several warming and cooling centers, sloping from 30 m to 80 m (from left to right) (Figure 9g). As for salinity, horizontal advection caused the salinity between +112 km to +640 km (right side of the track) to rise and the salinity outward to fall, aligned with a V-shaped band of large freshening located in subsurface layer. However, it is surprising that the surface positive salinity anomaly and subsurface negative salinity anomaly were both strengthened after considering the effect of precipitation (Figure 10a,d,g). The vertical structure of horizontal advection's effect is complex to explain because its effect mostly relied on the detailed salinity distribution and current direction.

Vertical advection, consisting of both upwelling and downwelling, induced a near-track cooling and an outward warming (Figure 9b,e). In the subsurface layer, a strong cooling (salinity-increasing) band tilted from 40 m to 80 m (from −40 km to +120 km), which suggested that the upwelling at the left side was stronger than that at the right side of TC track. When adding precipitation, the positive salinity anomaly was shallower than that in the no precipitation case (Figure 10b,e,h). As positive

anomaly caused by upwelling usually exists at the bottom of mixed layer, where vertical temperature gradient is greatest, it indicates that the mixed layer depth was shallower in the simulation with precipitation than that without precipitation.

Vertical mixing caused the strongest responses and differences between Pre and Nopre. It induced a strong surface cooling and V-shaped subsurface warming (Figure 9c,f), as well as an increase of surface salinity and a V-shaped decrease band of subsurface salinity (Figure 10c,f). The precipitation added in Pre caused obvious surface warming and subsurface cooling (Figure 9i), which may arise from the decreased vertical mixing. However, the salty layer became shallower and wider under the influence of precipitation (Figure 10i). Additionally, the range of freshening band in subsurface layer was also expanded. The differences in temperature anomaly between Pre and Nopre cases explain the indirect effect of precipitation. The fresh water injected by precipitation diluted the mixed layer, enhanced the stratification, results in a shallower mixed layer depth in Pre case that the Nopre case, which explains why the surface cold anomaly and subsurface warm anomaly in Pre case were weaker than the Nopre case (Figure 9i).
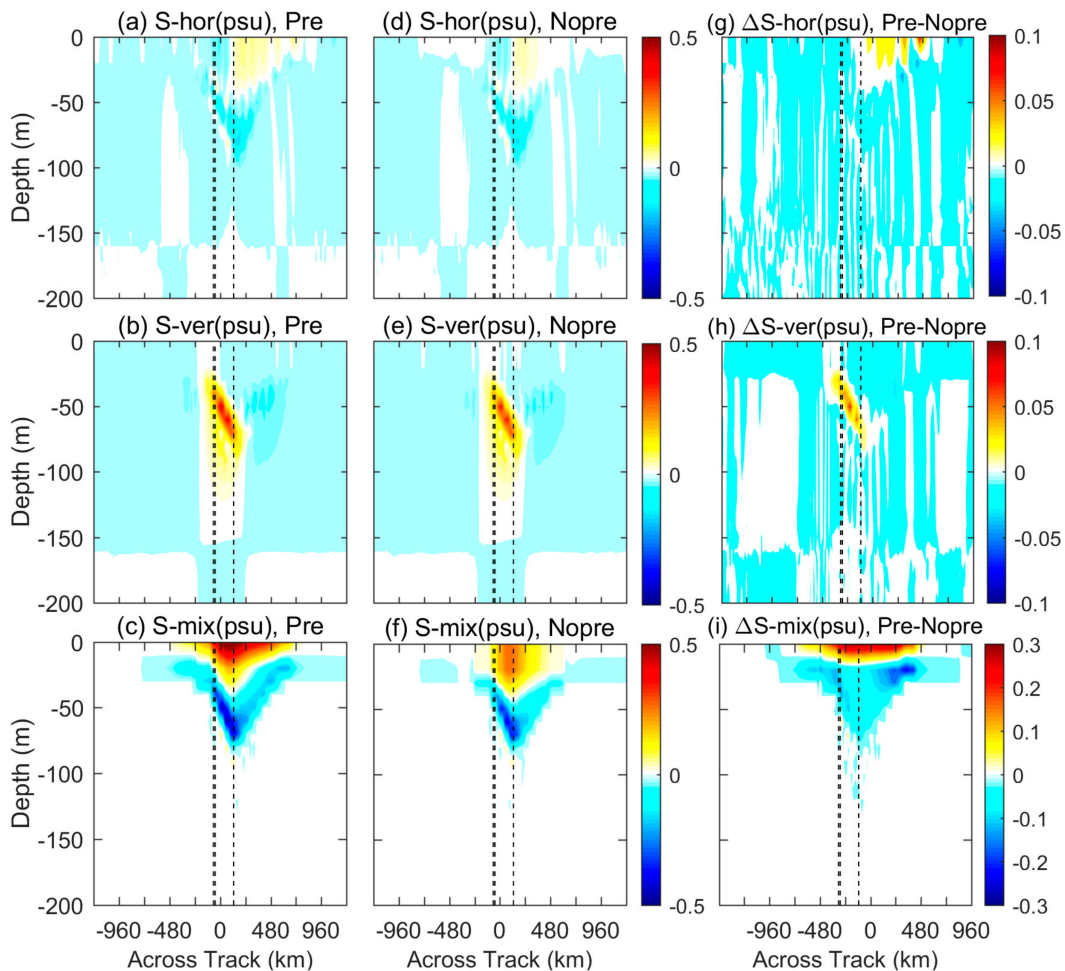
Figure 10. Same as in Figure 9 but for salinity.

Figure 11 shows the model simulated post-storm average temperature anomaly and salinity anomaly in the whole field. The across-track structure of salinity anomaly and temperature anomaly induced by Kalmaegi was similar with each other. It is the vertical mixing that dominated the responses above 100 m, leaving a cool-warm temperature anomaly and salty-fresh salinity anomaly structure (Figure 11a,b,e,f). In the surface layer (above 50 m), the response showed rightward-biased cooling and increase of salinity, which is the combined effect of vertical mixing and horizontal advection (Figure 9a,c,d,f and Figure 11e,f). In the subsurface layer (50–100 m), the left part of the "double-wing"

of warm anomaly and decrease in salinity caused by vertical mixing were suppressed by the cold and saline water brought by upwelling, while the right part keeps the response characteristics caused by vertical mixing (Figure 9b,c,e,f and Figure 11e,f). This cross-track difference occurred because the vertical mixing is weaker on the left side of the track than on the right side, and the upwelling is relatively stronger than vertical mixing on the left side. The mixed layer was finally diluted under the direct and indirect effect of precipitation (Figure 11c). Meanwhile, a warm-cool temperature variation structure formed under the total effect of precipitation (Figure 11g).
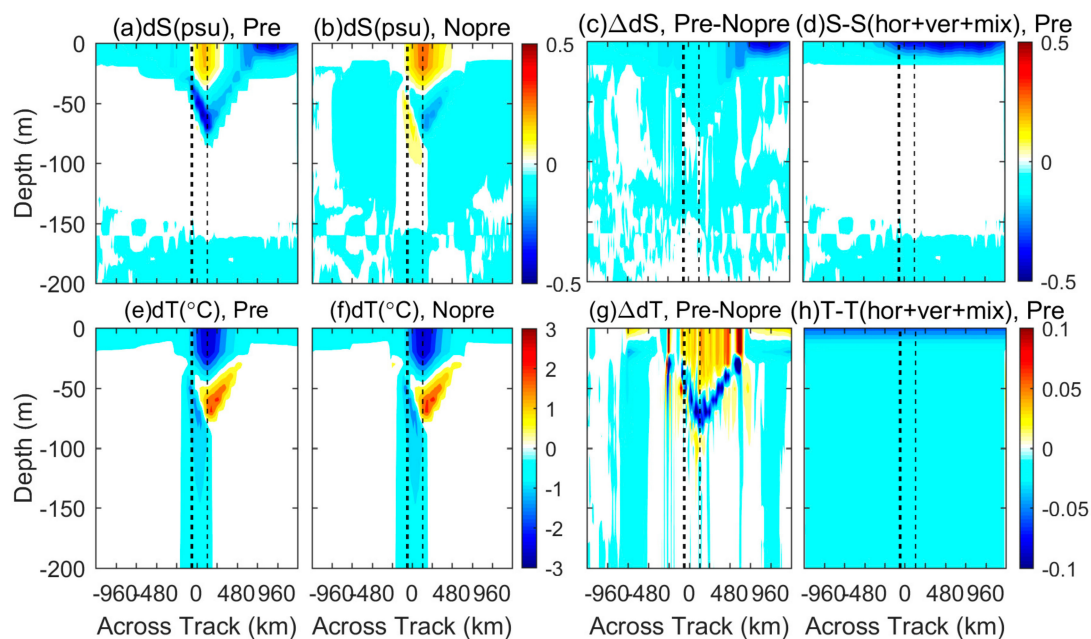
Figure 11. Post-storm average temperature anomaly and salinity anomaly in experiment (**a**,**e**) Pre, (**b**,**f**) Nopre, and (**c**,**g**) the corresponding differences between Pre and Nopre. (**d**,**h**) The value of difference calculated by the whole salinity (temperature) anomaly minus the sum of three components induced by three dynamic processes. The average is taken for the second to fifth inertial periods after the storm. The two dotted lines to the left of the track represent the positions of Stations 2 and 5. The dotted line at the right side represent the locations of Station 4.

In a summary, the vertical mixing was more sensitive to precipitation than the other processes. The temperature differences under the indirect effect of precipitation reflected that vertical mixing was suppressed by freshwater flux. However, when focus on the salinity caused by vertical mixing, it is interesting that the surface salty layer became shallower and wider under the influence of precipitation, and the range of negative salinity anomaly band in subsurface layer was also expanded (Figure 10c,f,i). Figure 11d shows the value of difference calculated by the whole salinity anomaly minus the sum of three components induced by three dynamic processes, which indicates that precipitation had a dilution effect on salinity. The difference is due to the setting of model output, because the effect of precipitation was added after the output of horizontal advection, vertical advection and vertical mixing. We will pay attention to this issue and design a more comprehensive simulation setting in our future studies.

The above analysis revealed that vertical mixing is likely to be an important way for precipitation to affect ocean conditions which requires great attention. In 3DPWP model, shear instability is mainly responsible for typhoon-induced vertical mixing. The vertical mixing discussed here is caused by shear flow instability and static instability rather than thermal instability. However, the thermal instability was not taken into account in this study because the model used in this study lacks of air-sea heat exchange processes, even though the thermal instability due to latent heat release at the air-sea interface

affect the entrainment rate at the mixed-layer base. Furthermore, the physical mechanism by which TC-precipitation plays a role still needs a great deal of in-depth research to explore.

4. Discussion and Conclusions

The atmospheric characteristics of Typhoon Kalmaegi (2014) and its induced upper ocean response have been studied in detail using multiple-satellite observations and in situ observations. More importantly, the role of TC precipitation on TC-induced upper ocean variations were also studied by using the 3DPWP model.

The asymmetric structure shown in the satellite IR images corresponds to the asymmetric distribution of the CMORPH precipitation. Different structures caused different responses when TC was passing over the observational stations. The wider and more convective cloud clusters on the left side of Kalmaegi's track caused stronger precipitation at Station 5 than at the other stations. The evolution of meteorological elements at the three stations during the passage of Kalmaegi had also been documented. When the typhoon eye passed by, the air pressure and relative humidity decreased, while the air temperature increased rapidly. Additionally, the maximum wind speed appeared twice when the annular eyewall passed.

Comparing the temperature profiles before and after Kalmaegi, the water column at Stations 2 and 5 were cooled, while a cooling-warming-cooling vertical structure appeared at Station 4. Those vertical profiles indicated that the upwelling is stronger than the vertical mixing at Stations 2 and 5, while the vertical mixing at Station 4 is strong enough to reach the depth affected by upwelling. The MLS became saltier at Station 4, while the salinity at Stations 2 and 5 experienced several dilution processes that were related to the intense precipitation. The strongest SSS increase at Station 4 was approximately 0.176 psu, and the strongest SSS decreases (increases) at Stations 2 and 5 were 0.145 psu (0.155 psu) and 0.278 psu (0.103 psu), respectively. It is uncertain whether the salinity response had the same rightward bias feature similar to temperature. All these differences between salinity and temperature responses prompt us to think about the dynamic differences that dominate these variations.

The 3DPWP model was capable to simulate the upper ocean variations regardless of the precipitation forcing. However, the simulation results with precipitation input is fresher and warmer. When precipitation was added to the model, the overestimation of SSS in the simulation without rainfall was suppressed. A model-based analysis suggests that considering precipitation in the 3DPWP model may cause the surface salinity to be fresher and the temperature to be slightly warmer. The mean ratios of impact within seven days after the forced stage were approximately 3.8%, 15.1%, and 2.7% (63.6%, 52.6%, and 63.0%) for the SST (SSS) at Stations 2, 4, and 5, respectively. Precipitation had a larger effect on salinity than on temperature, that is, salinity was more sensitive to precipitation than temperature. The precipitation is likely to work by changing the salinity stratification and impact the static stability, thus influencing vertical mixing and other internal ocean currents. The temperature variation induced by TC precipitation was a reflection of the above process.

The results of our study highlight the importance of precipitation for the TC-induced upper ocean response, especially for the ocean salinity. The SSS reduction during Kalmaegi, indicates that the effect of precipitation can be stronger than that of vertical mixing. Precipitation can directly reduce ocean salinity by adding freshwater into the ocean. Once the salinity becomes lower, the stratification would enhance, resulting in a shallower mixed layer depth and a weaker vertical mixing. Then the SST cooling would be suppressed because of the weakening vertical mixing. The weakened sea surface cooling caused by the enhanced upper-ocean stratification can in turn promote the TC to intensify and increase the vertical turbulent mixing. It looks like this forms a complete negative feedback process. Actually, the air-sea interaction during a TC is a complicated system in which multiple factors work together. Once precipitation occurs, the intensity, TC translation speed and other factors are constantly changed, which will also have an impact on the effect of precipitation. What's more, water vapor transfers energy from the ocean to the atmosphere, and then returns to the ocean in the form of precipitation, changes the ocean conditions, and further feed back into the atmosphere above it. In a

word, precipitation is very important for air-sea interaction during TCs, and the effect of precipitation (or freshwater flux) during a TC period should be taken seriously.

The model simulation in this study is an idealized test. Factors such as lack of surface heat flux and evaporation, inaccurate atmospheric forcing fields, and lack of atmospheric feedback mechanisms for ocean variations all affected the simulations. Therefore, a comprehensive ocean-atmosphere coupled model will be used to investigate the role of TC precipitation in TC-ocean response. Moreover, the impact of precipitation is likely concentrated in the mixed layer, so it is essential to choose a higher vertical resolution in the ocean model.

Author Contributions: H.Z. and J.M. put forward the idea and designed the research procedure; D.C. hosted the project which set the cross-shaped observational array in SCS; H.Z. and D.C. supervised the model simulation and data analysis of this manuscript; F.L. analyzed the data, conducted numerical simulations, visualized figures and wrote the manuscript; H.Z. assisted in data processing and analysis of in situ data and numerical simulations; J.M. helped to process satellite remote sensing data; H.Z., J.M., J.Z., and D.T. revised the manuscript and provide beneficial suggestions. All authors have read and agreed to the published version of the manuscript.

References

1. Jacob, S.D.; Shay, L.K.; Mariano, A.J.; Black, P.G. The 3D oceanic mixed layer response to Hurricane Gilbert. *J. Phys. Oceanogr.* **2000**, *30*, 1407–1429. [CrossRef]

2. Price, J.F. Upper ocean response to a Hurricane. *J. Phys. Oceanogr.* **1981**, *11*, 153–175. [CrossRef]

3. Yue, X.; Zhang, B.; Liu, G.; Li, X.; Zhang, H.; He, Y. Upper ocean response to typhoon Kalmaegi and Sarika in the South China Sea from multiple-satellite observations and numerical simulations. *Remote Sens.* **2018**, *10*, 348. [CrossRef]

4. Zhang, H.; Chen, D.; Zhou, L.; Liu, X.; Ding, T.; Zhou, B. Upper ocean response to typhoon Kalmaegi (2014). *J. Geophys. Res. Ocean.* **2016**, *121*, 6520–6535. [CrossRef]

5. Chiang, T.-L.; Wu, C.-R.; Oey, L.-Y. Typhoon Kai-Tak: An ocean's perfect storm. *J. Phys. Oceanogr.* **2011**, *41*, 221–233. [CrossRef]

6. Glenn, S.M.; Miles, T.N.; Seroka, G.N.; Xu, Y.; Forney, R.K.; Yu, F.; Roarty, H.; Schofield, O.; Kohut, J. Stratified coastal ocean interactions with tropical cyclones. *Nat. Commun.* **2016**, *7*, 10887. [CrossRef]

7. Black, W.J.; Dickey, T.D. Observations and analyses of upper ocean responses to tropical storms and hurricanes in the vicinity of Bermuda. *J. Geophys. Res.* **2008**, *113*, C08009. [CrossRef]

8. Cheng, L.; Zhu, J.; Sriver, R.L. Global representation of tropical cyclone-induced short-term ocean thermal changes using Argo data. *Ocean Sci.* **2015**, *11*, 719–741. [CrossRef]

9. Ning, J.; Xu, Q.; Feng, T.; Zhang, H.; Wang, T. Upper Ocean Response to Two Sequential Tropical Cyclones over the Northwestern Pacific Ocean. *Remote Sens.* **2019**, *11*, 2431. [CrossRef]

10. Zhang, H.; Liu, X.; Wu, R.; Liu, F.; Yu, L.; Shang, X.; Qi, Y.; Wang, Y.; Song, X.; Xie, X.; et al. Ocean Response to Successive Typhoons Sarika and Haima (2016) Based on Data Acquired via Multiple Satellites and Moored Array. *Remote Sens.* **2019**, *11*, 2360. [CrossRef]

11. Price, J.F.; Sanford, T.B.; Forristall, G.Z. Forced stage response to a moving Hurricane. *J. Phys. Oceanogr.* **1994**, *24*, 233–260. [CrossRef]

12. Emanuel, K.A. An air-sea interaction theory for tropical cyclones. Part I: Steady-state maintenance. *J. Atmos. Sci.* **1986**, *43*, 585–605. [CrossRef]

13. Emanuel, K.A. Thermodynamic control of hurricane intensity. *Nature* **1999**, *401*, 665–669. [CrossRef]

14. Bender, M.A.; Ginis, I.; Kurihara, Y. Numerical simulations of tropical cyclone-ocean interaction with a high-resolution coupled model. *J. Geophys. Res.* **1993**, *98*, 23245–23263. [CrossRef]

15. Emanuel, K.; Desautels, C.; Holloway, C.; Korty, R. Environmental control of tropical cyclone intensity. *J. Geophys. Res.* **2004**, *106*, 14771–14781. [CrossRef]

16. Cooper, N.S. The effect of salinity on tropical ocean models. *J. Phys. Oceanogr.* **1988**, *18*, 697–707. [CrossRef]

17. Jourdain, N.C.; Lengaigne, M.; Vialard, J.; Madec, G.; Menkes, C.E.; Vincent, E.M.; Jullien, S.; Barnier, B. Observation-based estimates of surface cooling inhibition by heavy rainfall under tropical cyclones. *J. Phys. Oceanogr.* **2013**, *43*, 205–221. [CrossRef]

18. Kil, B.; Burrage, D.; Wesson, J.; Howden, S. Sea surface signature of tropical cyclones using microwave remote sensing. In Occean Sensing and Monitoring V, Proceedings of the SPIE Defense, Security, and Sensing, Baltimore, MD, USA, 29 April–3 May 2013; SPIE: Baltimore, MD, USA, 2013; Volume 8724, pp. 1–15. [CrossRef]

19. Miller, J.R. The salinity effect in a mixed layer ocean model. *J. Phys. Oceanogr.* **1976**, *6*, 29–35. [CrossRef]

20. Vissa, N.K.; Satyanarayana, A.N.V.; Kumar, B.P. Response of upper ocean and impact of barrier layer on Sidr cyclone induced sea surface cooling. *Ocean Sci. J.* **2013**, *48*, 279–288. [CrossRef]

21. Lukas, R.; Lindstrom, E. The mixed layer of the western equatorial Pacific Ocean. *J. Geophys. Res.* **1991**, *96*, 3343–3357. [CrossRef]

22. Sprintall, J.; Tomczak, M. Evidence of the barrier layer in the surface layer of the tropics. *J. Geophys. Res.* **1992**, *97*, 7305–7316. [CrossRef]

23. Balaguru, K.; Chang, P.; Saravanan, R.; Leung, L.R.; Xu, Z.; Li, M.; Hsieh, J.S. Ocean barrier layers' effect on tropical cyclone intensification. *Proc. Natl. Acad. Sci. USA* **2012**, *109*, 14343–14347. [CrossRef]

24. Perigaud, C. Impact of interannual rainfall anomalies on Indian Ocean salinity and temperature variability. *J. Geophys. Res.* **2003**, *108*, 3319. [CrossRef]

25. Yan, Y.; Li, L.; Wang, C. The effects of oceanic barrier layer on the upper ocean response to tropical cyclones. *J. Geophys. Res. Ocean.* **2017**, *122*, 4829–4844. [CrossRef]

26. Neetu, S.; Lengaigne, M.; Vincent, E.M.; Vialard, J.; Madec, G.; Samson, G.; Ramesh Kumar, M.R.; Durand, F. Influence of upper-ocean stratification on tropical cyclone-induced surface cooling in the Bay of Bengal. *J. Geophys. Res. Ocean.* **2012**, *117*, C12020. [CrossRef]

27. Bond, N.A.; Cronin, M.F.; Sabine, C.; Kawai, Y.; Ichikawa, H.; Freitag, P.; Ronnholm, K. Upper ocean response to Typhoon Choi-Wan as measured by the kuroshio extension observatory mooring. *J. Geophys. Res.* **2011**, *116*, C02031. [CrossRef]

28. Domingues, R.; Goni, G.; Bringas, F.; Lee, S.K.; Kim, H.S.; Halliwell, G.; Dong, J.; Morell, J.; Pomales, L. Upper ocean response to Hurricane Gonzalo (2014): Salinity effects revealed by targeted and sustained underwater glider observations. *Geophys. Res. Lett.* **2015**, *42*, 7131–7138. [CrossRef]

29. Chaudhuri, D.; Sengupta, D.; D'Asaro, E.; Venkatesan, R.; Ravichandran, M. Response of the salinity-stratified Bay of Bengal to cyclone Phailin. *J. Phys. Oceanogr.* **2019**, *49*, 1121–1140. [CrossRef]

30. Liu, Z.; Xu, J.; Zhu, B.; Sun, C.; Zhang, L. The upper ocean response to tropical cyclones in the northwestern Pacific analyzed with Argo data. *Chin. J. Oceanol. Limnol.* **2007**, *25*, 123–131. [CrossRef]

31. Grodsky, S.A.; Reul, N.; Lagerloef, G.; Reverdin, G.; Carton, J.A.; Chapron, B.; Quilfen, Y.; Kudryavtsev, V.N.; Kao, H.Y. Haline hurricane wake in the Amazon/Orinoco plume: AQUARIUS/SACD and SMOS observations. *Geophys. Res. Lett.* **2012**, *39*, L20603. [CrossRef]

32. Liu, Z.; Xu, J.; Sun, C.; Wu, X. An upper ocean response to Typhoon Bolaven analyzed with Argo profiling floats. *Acta Oceanol. Sin.* **2014**, *33*, 90–101. [CrossRef]

33. Brand, S. The effects on a tropical cyclone of cooler surface waters due to upwelling and mixing produced by a prior tropical cyclone. *J. Appl. Meteorol.* **1971**, *10*, 865–874. [CrossRef]

34. Lin, I.I.; Wu, C.-C.; Pun, I.-F.; Ko, D.-S. Upper-ocean thermal structure and the Western North Pacific category 5 Typhoons. Part I: Ocean features and the category 5 Typhoons' intensification. *Monthly Weather Rev.* **2008**, *136*, 3288–3306. [CrossRef]

35. Sandery, P.A.; Brassington, G.B.; Craig, A.; Pugh, T. Impacts of ocean–atmosphere coupling on tropical cyclone intensity change and ocean prediction in the Australian region. *Monthly Weather Rev.* **2010**, *138*, 2074–2091. [CrossRef]

36. Lin, S.; Zhang, W.-Z.; Shang, S.-P.; Hong, H.-S. Ocean response to typhoons in the western North Pacific: Composite results from Argo data. *Deep Sea Res. Part I Oceanogr. Res. Pap.* **2017**, *123*, 62–74. [CrossRef]

37. Vincent, E.M.; Lengaigne, M.; Vialard, J.; Madec, G.; Jourdain, N.C.; Masson, S. Assessing the oceanic control on the amplitude of sea surface cooling induced by tropical cyclones. *J. Geophys. Res. Ocean.* **2012**, *117*, C05023. [CrossRef]

38. Maneesha, K.; Murty, V.S.N.; Ravichandran, M.; Lee, T.; Yu, W.; McPhaden, M.J. Upper ocean variability in the Bay of Bengal during the tropical cyclones Nargis and Laila. *Prog. Oceanogr.* **2012**, *106*, 49–61. [CrossRef]

39. Ning, J.; Xu, Q.; Zhang, H.; Wang, T.; Fan, K. Impact of Cyclonic Ocean Eddies on Upper Ocean Thermodynamic Response to Typhoon Soudelor. *Remote Sens.* **2019**, *11*, 938. [CrossRef]

40. Delcroix, T.; Henin, C.; Porte, V.; Arkin, P. Precipitation and sea-surface salinity in the tropical Pacific Ocean. *Deep Sea Res. Part I Oceanogr. Res. Pap.* **1996**, *43*, 1123–1141. [CrossRef]

41. McPhaden, M.J.; Foltz, G.R.; Lee, T.; Murty, V.S.N.; Ravichandran, M.; Vecchi, G.A.; Vialard, J.; Wiggert, J.D.; Yu, L. Ocean-atmosphere interactions during Cyclone Nargis. *EOS Trans. AGU* **2009**, *90*, 53–54. [CrossRef]

42. Dessier, A.; Donguy, J.R. The sea surface salinity in the tropical Atlantic between 10°S and 30°N—Seasonal and interannual variations (1977–1989). *Deep Sea Res. Part I Oceanogr. Res. Pap.* **1994**, *41*, 81–100. [CrossRef]

43. Bingham, F.M.; Foltz, G.R.; McPhaden, M.J. Seasonal cycles of surface layer salinity in the Pacific Ocean. *Ocean Sci.* **2010**, *6*, 775–787. [CrossRef]

44. Hsu, P.-C.; Ho, C.-R. Typhoon-induced ocean subsurface variations from glider data in the Kuroshio region adjacent to Taiwan. *J. Oceanogr.* **2019**, *75*, 1–21. [CrossRef]

45. Jacob, S.D.; Koblinsky, C.J. Effects of precipitation on the upper-ocean response to a Hurricane. *Monthly Weather Rev.* **2007**, *135*, 2207–2225. [CrossRef]

46. Zhang, H.; Wu, R.; Chen, D.; Liu, X.; He, H.; Tang, Y.; Ke, D.; Shen, Z.; Li, J.; Xie, J.; et al. Net modulation of upper ocean thermal structure by Typhoon Kalmaegi (2014). *J. Geophys. Res. Ocean.* **2018**, *123*, 7154–7171. [CrossRef]

47. Ying, M.; Zhang, W.; Yu, H.; Lu, X.; Feng, J.; Fan, Y.; Zhu, Y.; Chen, D. An overview of the China meteorological administration tropical cyclone database. *J. Atmos. Ocean. Technol.* **2014**, *31*, 287–301. [CrossRef]

48. The China Meteorological Administration (CMA) Tropical Cyclone Best Track Dataset. Available online: http://tcdata.typhoon.org.cn/zjljsjj_sm.html (accessed on 26 October 2017).

49. Liang, J.; Ren, F.; Yang, X. Study on the differences between CMA and JTWC tropical cyclone datasets for northwest Pacific. *Acta Oceanol. Sin.* **2010**, *32*, 10–22. (In Chinese)

50. Ren, F.; Liang, J.; Wu, G.; Dong, W.; Yang, X. Reliability analysis of climate change of tropical cyclone activity over the Western North Pacific. *J. Clim.* **2011**, *24*, 5887–5898. [CrossRef]

51. Barnes, W.L.; Puschell, J.J.; Lowe, H.A.; Jeter, J.W.; Kus, S.M.; Hurt, W.T.; Gilman, D.; Rogers, D.L.; Hoelter, R.L.; Ravella, R. Japanese advanced meteorological imager: A next generation GEO imager for MTSAT-1R. *Proc. SPIE* **2002**, *4814*, 152–161. [CrossRef]

52. Yi, L.; Thies, B.; Zhang, S.; Shi, X.; Bendix, J. Optical thickness and effective radius retrievals of low stratus and fog from MTSAT daytime data as a prerequisite for Yellow Sea Fog detection. *Remote Sens.* **2015**, *8*, 8. [CrossRef]

53. Geo-Coordinate Mapped Data for Almost ALL Area GMS/MTSAT Covers. Available online: http://weather.is.kochi-u.ac.jp/archive-e.html (accessed on 26 October 2017).

54. NOAA CPC Morphing Technique ("CMORPH") Data. Available online: https://www.cpc.ncep.noaa.gov/products/janowiak/cmorph_description.html (accessed on 15 November 2017).

55. Joyce, R.J.; Janowiak, J.E.; Arkin, P.A.; Xie, P. CMORPH: A method that produces global precipitation estimates from passive microwave and infrared data at high spatial and temporal resolution. *J. Hydrometeorol.* **2004**, *5*, 487–503. [CrossRef]

56. Wu, Q.; Wang, Y. Comparison of oceanic multisatellite precipitation data from tropical rainfall measurement mission and global precipitation measurement mission datasets with rain gauge data from ocean buoys. *J. Atmos. Ocean. Technol.* **2019**, *36*, 903–920. [CrossRef]

57. Price, J.F.; Weller, R.A.; Pinkel, R. Diurnal cycling: Observations and models of the upper ocean response to diurnal heating, cooling, and wind mixing. *J. Geophys. Res.* **1986**, *91*, 8411–8427. [CrossRef]

58. Sanford, T.B.; Price, J.F.; Girton, J.B.; Webb, D.C. Highly resolved observations and simulations of the ocean response to a Hurricane. *Geophys. Res. Lett.* **2007**, *34*, L13604. [CrossRef]

59. Guan, S.; Zhao, W.; Huthnance, J.; Tian, J.; Wang, J. Observed upper ocean response to Typhoon Megi (2010) in the Northern South China Sea. *J. Geophys. Res. Ocean.* **2014**, *119*, 3134–3157. [CrossRef]

60. Jelesnianski, C.P. Numerical computations of storm surges without bottom stress. *Monthly Weather Rev.* **1966**, *94*, 379–394. [CrossRef]

61. Oey, L.Y.; Ezer, T.; Wang, D.P.; Fan, S.J.; Yin, X.Q. Loop current warming by Hurricane Wilma. *Geophys. Res. Lett.* **2006**, *33*, L08613. [CrossRef]

62. Chien, F.-C.; Liu, Y.-C.; Lee, C.-S. Heavy rainfall and southwesterly flow after the leaving of Typhoon Mindulle (2004) from Taiwan. *J. Meteorol. Soc. Jpn.* **2008**, *86*, 17–41. [CrossRef]

63. Chien, F.-C.; Kuo, H.-C. On the extreme rainfall of Typhoon Morakot (2009). *J. Geophys. Res.* **2011**, *116*, D05104. [CrossRef]

64. Corbosiero, K.L.; Molinari, J. The relationship between storm motion, vertical wind shear, and convective asymmetries in tropical cyclones. *J. Atmos. Sci.* **2003**, *60*, 366–376. [CrossRef]

65. Xu, W.; Jiang, H.; Kang, X. Rainfall asymmetries of tropical cyclones prior to, during, and after making landfall in South China and Southeast United States. *Atmos. Res.* **2014**, *139*, 18–26. [CrossRef]

66. Willoughby, H.E. Tropical cyclone eye thermodynamics. *Monthly Weather Rev.* **1998**, *126*, 3053–3067. [CrossRef]

67. Sun, L.; Li, Y.X.; Yang, Y.J.; Wu, Q.Y.; Chen, X.T.; Li, Q.Y.; Li, Y.B.; Xian, T. Effects of super typhoons on cyclonic ocean eddies in the western North Pacific: A satellite data-based evaluation between 2000 and 2008. *J. Geophys. Res. Ocean.* **2014**, *119*, 5585–5598. [CrossRef]

68. Liu, S.S.; Sun, L.; Wu, Q.Y.; Yang, Y.J. The responses of cyclonic and anticyclonic eddies to typhoon forcing: The vertical temperature-salinity structure changes associated with the horizontal convergence/divergence. *J. Geophys. Res. Ocean.* **2017**, *122*, 4974–4989. [CrossRef]